

# In Vitro Design Investigation of a Rotating Helical Magnetic Swimmer for Combined 3D Navigation and Blood Clot Removal

Julien Leclerc, *Member, IEEE*, Haoran Zhao, Daniel Bao and Aaron T. Becker, *Senior Member, IEEE*

**Abstract**—This paper presents a miniature magnetic swimmer and a control apparatus able to perform both 3D path following and blood clot removal. The robots are 2.5 mm in diameter, 6 mm in length, contain an internal permanent magnet, and have cutting tips coated in diamond powder. The robots are magnetically propelled by an external magnetic system using three coil pairs arranged orthogonally. A range of robot tip designs were tested for abrading human blood clots *in vitro*. The best design removed a blood clot at a maximum rate of 20.13 mm<sup>3</sup>/min. A controller for 3D navigation is presented and tested. The best prototype was used in an experiment that combined both 3D path following and blood clot removal.

## I. INTRODUCTION

Coagulation, also called *blood clotting*, is a biological process that stops blood leakage after a vein or artery is damaged by forming a blood clot. Coagulation is desirable; however, excessive coagulation can lead to serious health problems. A *thrombus* is a blood clot formed inside a blood vessel. Thrombi can form inside veins or arteries. It is estimated that one to two persons per thousand is adversely affected by a venous thrombosis every year [1]–[6]. Arterial thromboembolism is much more prevalent and fatal, affecting around 18 persons per thousand [7]. Thrombi are usually treated using clot-dissolving medication (thrombolysis) or mechanically removed using a catheter [8]–[11]. These methods have drawbacks for some patients. Thrombolytic medication can produce life-threatening bleeding if other injuries occur to the patient [12], [13]. Catheters are long tubes inserted inside arteries or veins and are guided by special imaging equipment. They rub against the walls of arteries during insertion and retraction and may detach arterial plaques (calcified fat deposits) that can travel within the bloodstream and produce a blockage elsewhere [14], [15].

Miniature magnetic agents are currently being studied as a solution to these problems. These devices could navigate within the bloodstream of patients with reduced risks of damaging blood vessels because tetherless magnetic control is a compliant actuation method. The novelty introduced in the present paper is a magnetic swimmer design and an experimental apparatus able to perform both 3D closed-loop path-following and blood clot removal during the same

Authors are with the University of Houston, Department of Electrical and Computer Engineering.

Manuscript received January 14, 2019; revised December 9, 2019; accepted March 15, 2020. Date of current version April 14, 2020. This paper was recommended for publication by Editor Mark Yim upon evaluation of the reviewers comments.

The raw data and code for the project is available at <https://github.com/RoboticSwarmControl/MagneticSwimmer-3DNav-BloodClot>.

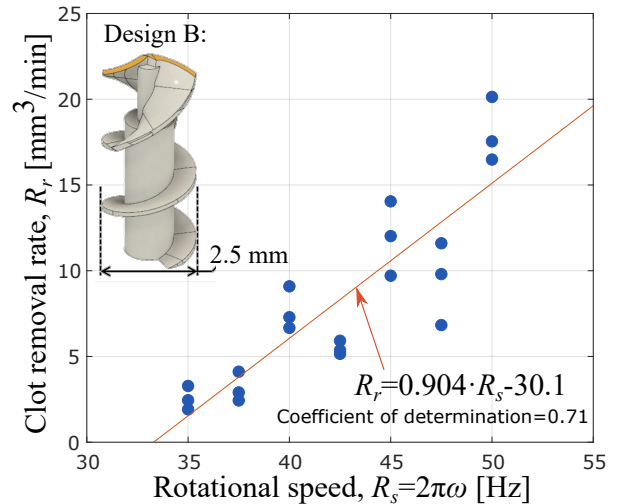


Fig. 1. Plot of blood clot removal rate as a function of rotational speed for design B, the swimmer prototype that removed clots the fastest. The CAD model of this swimmer is also shown.

experiment (see Fig. 7).

Many types of magnetic robots have been designed and tested for navigation. Hu et al. created a rectangular-sheet-shaped robot made of a flexible magnetic material. This agent could achieve many modes of locomotion, including walking, swimming, rolling, or jumping [16]. Vollmers et al. invented a wireless resonant magnetic microactuator (WRMM) powered by the combination of a magnetic field and a clamping voltage oscillating at frequencies in the range of 2 to 3 kHz [17]. Onaizah et al. recently introduced magnetically actuated scissors that can achieve both locomotion and cutting movements [18].

Rotating magnetic swimmers have been studied as a solution to remove blood clots to treat conditions such as pulmonary or cardiac embolisms. The rotational movement can be used to abrade clots [19]–[22] and to generate a propulsive force by using a swimmer that has a helical shape [23]–[31]. Khalil et al. experimentally demonstrated that a helical swimmer having a diameter of 0.3 mm and a length of 4 mm was able to remove human blood clots at a speed of 0.614 mm<sup>3</sup>/s [21]. The position of the swimmer was regulated in 1D by using an ultrasound scanner to sense the position of the agent. This group also modeled the rubbing of helical swimmers on blood clots [32]. Open-loop 3D control was achieved by Sunky et al., who fabricated a millimeter-scale rotating swimmer able to navigate inside an artificial 3D vasculature and remove thrombi models [33]. Closed-loop 3D control of helical magnetic swimmers inside high

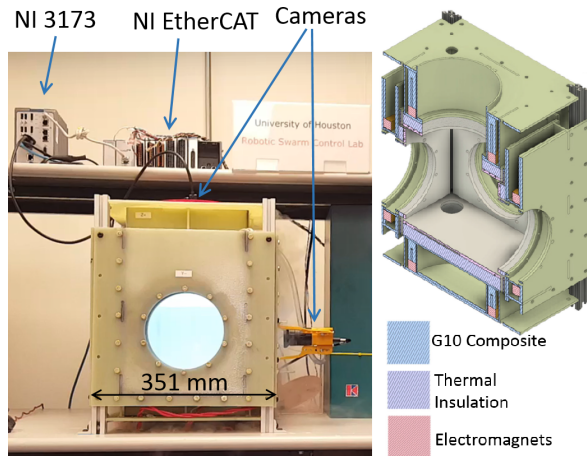


Fig. 2. Picture of the magnetic manipulator and its electronic system (left). CAD drawing of the magnetic manipulator (right).

viscosity fluids was recently achieved [34]–[36].

A clot removal procedure using a miniature swimmer requires several steps: (1) insertion of the swimmer, (2) navigation toward the thrombus, (3) removal of the thrombus, (4) navigation toward the retrieval point, (5) retrieval of the swimmer. This paper presents in vitro studies of steps (2) and (3). Human blood clots were made inside artificial blood vessels and removed with different swimmer designs and with different magnetic field rotational speeds. The clot removal rate was measured for these swimmer designs. The results were used to determine a relationship between the magnetic field rotational speed and the removal rate. The swimmer with the largest removal rate was then used to accurately follow a 3D path to a blood clot and completely remove the clot.

## II. MATERIAL AND METHODS

This section describes the hardware used for the experiments as well as the methods used to calculate the current to apply to each electromagnet.

### A. Hardware

**Magnetic manipulator:** The magnetic manipulator is a lab-built robotic system able to control miniature swimmers in 3D [37]. A picture and a 3D drawing are shown in Fig. 2. It produces a magnetic field to apply a torque or a force on a magnetic object. The magnitude, direction, and gradient of the field can be controlled in 3D using an inverse magnetic calculation. The manipulator can control magnetic robots in a cube-shaped workspace with a side length of 150 mm. It has six electromagnets placed in cubical shape. A distance of 300 mm separates the electromagnets on opposite sides. Current-mode power supplies are used to power the electromagnets. In this mode, each power supply internally performs a current regulation. It is advantageous to control the current circulating inside the electromagnets rather than the voltage because the magnetic field produced is proportional to the current. The power system can provide 20 A and 100 V to each electromagnet (12 kW total power). Each coil is

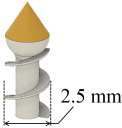
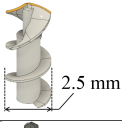
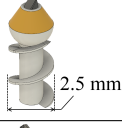
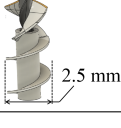


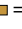
Swimmer Design	Removal rate in mm <sup>3</sup> /min	Remarks
A: 	0.3	Experiment was stopped after 14 min due to slow progress. Incomplete clot removal.
B: 	12.3	A blood clot with volume of 50 mm <sup>3</sup> completely removed.
C: 	1.76	Experiment was stopped after 14 min due to slow progress. Incomplete clot removal.
D: 	10.3	Experiment was stopped after 4 min because swimmer became stuck in the clot and stopped rotating.

TABLE I

COMPARISON BETWEEN THE REMOVAL RATE OF DIFFERENT SWIMMER DESIGNS AT 45 HZ. A SINGLE TEST WAS PERFORMED FOR EACH DESIGN. DESIGN B HAS THE HIGHEST REMOVAL RATE.

LEGEND:  = DIAMOND POWDER,  = ACRYLATE,  = DRILL BIT.

connected to a set of two Kepco BOP 20-50 (20 A, 50 V) power supplies connected in series. An industrial controller IC 3173 manufactured by National Instruments (NI) is used for real-time computation. Position feedback is obtained using two Basler acA800 cameras (800×600 resolution, 511 FPS max) placed on orthogonal sides of the workspace. The computer program only acquires images at a rate of 100 FPS. An NI Ethercat input/output interface produces six analog outputs to control the power supplies.

**Swimmer designs and fabrication:** The swimmer designs A–D in Table I are each made of three components: a 3D-printed body, a cylindrical permanent magnet, and a clot removing tip. The body has helical fins. It contains a tubular section to receive the permanent magnet. One side of the body has an abrasive coating. This side is specially shaped to promote abrasion. The bodies were fabricated using a ProJet 3510 HD. The abrasive coating is made of synthetic diamond powder (grain size 106–125 μm). The powder is bonded to the tip of the swimmer using 1-minute Loctite epoxy resin. This resin is not bio-compatible; however, bio-compatible epoxy resins are commercially available. Design C and D possess a 0.75 mm diameter drill bit on their tip. This element was added with the idea of increasing the swimmer anchorage inside the clot but proved to be ineffective. The cylindrical permanent magnets used for these swimmers are made of N50 NdFeB and are radially magnetized. The calculated maximum torque applied to the swimmer by the magnetic manipulator is equal to 126 μN·m. The magnets have a length of 1 mm and a diameter of 0.75 mm. They were dipped into the same epoxy resin used for the abrasive coating and inserted inside the tubular part of the swimmer.

The swimmers used for 3D navigation were partially painted black to facilitate computer vision detection.

### B. Calculation of the rotating magnetic field

Our rotating swimmers contain a cylindrical permanent magnet magnetized along the radial direction. When a rotating magnetic field is applied to these swimmers, they rotate and align their long axis with the rotational axis of the magnetic field. Their helical fins produce a force that propels the swimmer forward.

It is necessary to calculate the desired magnetic field in a Cartesian coordinate system  $XYZ$  orientated along the electromagnet's axis to use the inverse method described in [37]. A coordinate system  $UVW$  is defined at the swimmer's position, and we assume that the swimmer is aligned with the  $W$  axis. The magnetic field vector is generated in the  $UV$  plane, and rotates around the  $W$  axis. It is calculated using (1). The orientation of the swimmer is controlled by changing the orientation of  $UVW$  with respect to  $XYZ$ . The  $UVW$  coordinate system is rotated by an angle  $\alpha_x$  around axis  $X$  (rotation matrix 2), and by an angle  $\alpha_y$  around axis  $Y$  (rotation matrix 3). The magnetic field can be calculated in the  $XYZ$  coordinate system by combining (1), and (4).

$$\mathbf{B}_{uvw} = \begin{bmatrix} B_u \\ B_v \\ B_w \end{bmatrix} = B_0 \cdot \begin{bmatrix} \cos(\theta(t)) \\ \sin(\theta(t)) \\ 0 \end{bmatrix} \quad (1)$$

$$\mathbf{R}_x(\alpha_x) = \begin{bmatrix} 1 & 0 & 0 \\ 0 & \cos(\alpha_x) & -\sin(\alpha_x) \\ 0 & \sin(\alpha_x) & \cos(\alpha_x) \end{bmatrix} \quad (2)$$

$$\mathbf{R}_y(\alpha_y) = \begin{bmatrix} \cos(\alpha_y) & 0 & \sin(\alpha_y) \\ 0 & 1 & 0 \\ -\sin(\alpha_y) & 0 & \cos(\alpha_y) \end{bmatrix} \quad (3)$$

$$\mathbf{B}_{xyz} = \mathbf{R}_x(\alpha_x) \cdot \mathbf{R}_y(\alpha_y) \cdot \mathbf{B}_{uvw} \quad (4)$$

### C. Inverse magnetics

The inverse magnetic method calculates the current to apply to each electromagnet to produce the desired flux density  $\mathbf{B}_{xyz}$ . The flux density is the sum of the flux density produced by each electromagnet. The vector  $\mathbf{I}$  contains the current circulating inside each electromagnet:

$$\mathbf{I} = [I_1 \ I_2 \ I_3 \ I_4 \ I_5 \ I_6]^\top. \quad (5)$$

The flux density  $\mathbf{B}_{xyz}$  produced by the manipulator at the robot location  $\mathbf{P}$  is calculated using:

$$\mathbf{B}_{xyz} = \mathbf{A} \cdot \mathbf{I}, \quad (6)$$

where  $\mathbf{A}$  is the actuation matrix. The matrix  $\mathbf{A}$  is built using the following equations:

$$\mathbf{A} = \begin{bmatrix} \tilde{\mathbf{B}}_x(\mathbf{P}) \\ \tilde{\mathbf{B}}_y(\mathbf{P}) \\ \tilde{\mathbf{B}}_z(\mathbf{P}) \end{bmatrix}, \quad (7)$$

$$\tilde{\mathbf{B}}_x(\mathbf{P}) = [\tilde{B}_{1x}(\mathbf{P}) \ \tilde{B}_{2x}(\mathbf{P}) \ \tilde{B}_{3x}(\mathbf{P}) \ \tilde{B}_{4x}(\mathbf{P}) \ \tilde{B}_{5x}(\mathbf{P}) \ \tilde{B}_{6x}(\mathbf{P})], \quad (8)$$

$$\tilde{\mathbf{B}}_y(\mathbf{P}) = [\tilde{B}_{1y}(\mathbf{P}) \ \tilde{B}_{2y}(\mathbf{P}) \ \tilde{B}_{3y}(\mathbf{P}) \ \tilde{B}_{4y}(\mathbf{P}) \ \tilde{B}_{5y}(\mathbf{P}) \ \tilde{B}_{6y}(\mathbf{P})], \quad (9)$$

$$\tilde{\mathbf{B}}_z(\mathbf{P}) = [\tilde{B}_{1z}(\mathbf{P}) \ \tilde{B}_{2z}(\mathbf{P}) \ \tilde{B}_{3z}(\mathbf{P}) \ \tilde{B}_{4z}(\mathbf{P}) \ \tilde{B}_{5z}(\mathbf{P}) \ \tilde{B}_{6z}(\mathbf{P})]. \quad (10)$$

The coefficients  $\tilde{B}_{it}(\mathbf{P})$  correspond to the flux density produced per unit of current by electromagnet  $i$  on axis  $t$  where  $t$  can be equal to  $x$ ,  $y$ , or  $z$ . These coefficients are a function of the geometry of the electromagnets as well as the position of the swimmer in the workspace. The electromagnets are approximated by circular current loops, and the analytical equation presented in [38] is used to calculate the coefficients  $\tilde{B}_{it}(\mathbf{P})$ . To calculate the currents, it is necessary to inverse (6). The system is underdetermined as  $\mathbf{A}$  has a size  $3 \times 6$ . There are therefore an infinite number of solutions. Because matrix  $\mathbf{A}$  has linearly independent rows, the right pseudo-inverse (11) is performed to find a solution. This least norm solution minimizes the norm of  $\mathbf{I}$ , and therefore reduces the power lost by Joule effect in the electromagnets.

$$\mathbf{I} = \mathbf{A}^T (\mathbf{A} \cdot \mathbf{A}^T)^{-1} \cdot \mathbf{B}_{xyz} \quad (11)$$

### D. 3D closed-loop navigation

The swimmer was tested following a 3D closed path that was 316.5 mm long with eight turns having a minimum radius 10 mm and a maximum radius 40 mm. This path was generated using 39 waypoints. The waypoints were interpolated by a piecewise cubic spline to produce an array of points separated by a distance of 0.5 mm along the route. The camera system tracked the black-painted robot, producing  $\mathbf{P}_s(t)$ , a 3D position measurement at 100 Hz.

*Controller structure:* A block diagram of the controller used in this study is presented in Fig. 3. A similar controller is presented in [39]. After each robot position measurement, the closest waypoint to the robot,  $\mathbf{P}[i]$  was identified. The path controller determines  $\mathbf{u}(t)$ , the orientation of the magnetic field rotation axis. Two components are used to calculate  $\mathbf{u}(t)$ : the path following error ( $\mathbf{P}[i] - \mathbf{P}_s(t)$ ), and the (discretized) tangent to the path. There are two tuning parameters:  $\beta \in (0, \infty)$  to control the relative importance of path error and path tangent, and  $\gamma \in \mathbb{Z}^+$ , which determines the distance along the path to compute the tangent. Small values of  $\beta$  attempt to track a path waypoint but do not progress along the path well, while large  $\beta$  values result in paths that diverge from the waypoints (see Fig. 5). Because the waypoints are spaced every 0.5 mm, a  $\gamma$  of 1 sets a lookahead of 0.5 mm for the tangent calculation:

$$\mathbf{f}(t) = (\mathbf{P}[i] - \mathbf{P}_s(t)) + \beta \left( \frac{\mathbf{P}[i + \gamma] - \mathbf{P}[i]}{\|\mathbf{P}[i + \gamma] - \mathbf{P}[i]\|_2} \right) \quad (12)$$

$$\mathbf{u}(t) = \frac{\mathbf{f}(t)}{\|\mathbf{f}(t)\|_2} \quad (13)$$

$$\omega(t) = 160 \text{ rad/s}. \quad (14)$$

The magnetic axis direction  $\mathbf{u}(t)$  must then be converted to a pair of angles:

$$[\alpha_x(t), \alpha_y(t)] = [-\arctan2(\mathbf{u}_y(t), \mathbf{u}_z(t)), \sin^{-1}(\mathbf{u}_x(t))] \quad (15)$$

where  $\arctan2(y, z)$  calculates the arctangent of  $y/z$ . These equations, together with the methods described in the previous subsections, allow performing 3D path-following to

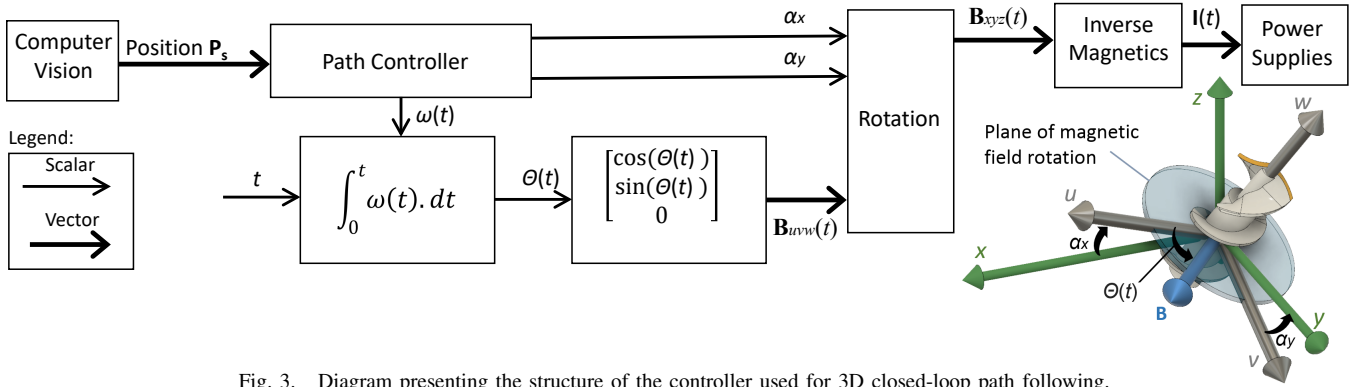


Fig. 3. Diagram presenting the structure of the controller used for 3D closed-loop path following.

reach a blood clot. The next step is the removal of this obstruction.

### E. Blood clot removal

*Artificial blood vessels fabrication:* To create suitable channels for a thrombus to form, we used a SYLGARD™ 184 PDMS (Poly-dimethyl siloxane) elastomer as a soft lithographic mold. PDMS is used in many applications, and many researchers have used PDMS to model blood vessel walls, e.g. [40]. The elastomer resin was cured in a 100 mm diameter Petri dish for one hour at 60° C with the manufacturer’s suggested curing ratio of 10 parts resin to 1 part curing agent. Three 3 mm diameter aluminum rods were used as blanks to form the channels. The surrounding PDMS was then cut to create a horizontal cross-section to remove the rods. Three channels were created to allow performing three blood clot removal tests at the same time. A magnetic simulation was performed using the software FEMM to quantify the magnetic field inhomogeneity, see Fig. 4. The simulation showed that the field is uniform at  $\pm 3.04\%$ . These PDMS channels were used to perform the blood clot removal tests presented in subsection III-B. For the combined navigation and blood clot removal experiment presented in Section IV a glass tube having an internal diameter of 3mm was used.

*Experimental protocol:* All blood clot removal experiments were performed using the following protocol. Blood was taken from a healthy volunteer using a sterile lancet and dispensed onto a clean Petri dish. A 60-minute timer was started just after the blood was drawn. Fifty  $\mu\text{L}$  of blood was then pipetted into each channel while being careful to avoid air bubbles. This process takes approximately five minutes. The blood formed a cylindrical column nearly 5 mm long. The side of the clots was approximately 10 mm away from the end of the channel. The artificial blood vessels were then placed into the magnetic manipulator which had been pre-heated to 37°C. The blood was left to coagulate at this temperature until five minutes were left in the timer. At that moment, the channels were taken out of the manipulator, and were filled with phosphate-buffered saline (PBS), to match the pH of blood. The channels were then placed back into the magnetic manipulator, and the clot removal tests were started when the timer had elapsed. The air temperature

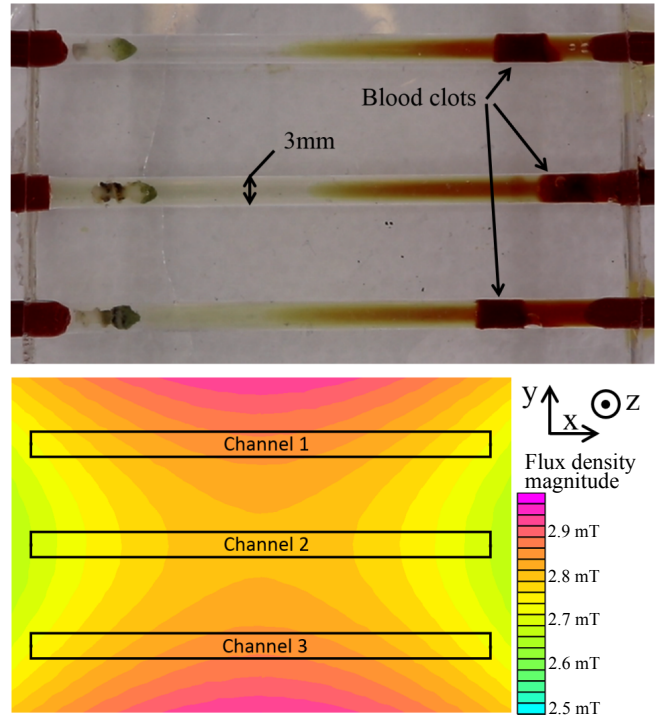


Fig. 4. Top: Picture of three swimmers inside PDMS channels at the beginning of a blood clot removal experiment, before the rotating magnetic field is activated. When the rotating field is applied, the swimmers move toward  $x+$  until they touch the blood clot, and start to abrade it. Bottom: Image of a magnetic simulation performed using the software FEMM. In this simulation, a current of 2 A circulates in the two electromagnets oriented along the  $y$ -axis. This simulation shows that the flux density is uniform at  $\pm 3.04\%$  over the channels. In the clot removal experiment, the flux density vector is in the  $y$ - $z$  plane, and rotates around the  $x$ -axis. This simulation is a snapshot of the flux density magnitude when the flux density vector is oriented along the  $y$ -axis.

inside the manipulator was regulated to 37°C during the clot removal tests. All Petri dishes and channels in contact with human blood were soaked and washed in bleach to prevent contamination, and other materials were disposed of in a biohazard or sharps disposal box.

A Canon EOS RebelSL2 camera was used to monitor the swimmers. The time taken by the swimmers to remove each clot was measured using a stopwatch. For clots that were completely removed, the removal rate was calculated

by dividing the initial clot volume by the time required to remove it. If the clot was not completely removed during the test, the removal rate was calculated manually from the recorded video.

### III. RESULTS

The results section focuses on *navigation*, used to reach either the thrombus or the retrieval point, and *removal* of the thrombus.

#### A. 3D closed-loop navigation

The swimmer was tested following a 3D closed path that was 316.5 mm long and had eight turns having a minimum radius of 10 mm and a maximum radius 40 mm. Different values for the controller parameters  $\gamma$  and  $\beta$  were tested and compared. Figure 5-A shows the paths followed by the swimmer when  $\gamma=1$  and  $\gamma=5$  with  $\beta=3.5$ . The swimmer velocity is  $100.5 \pm 4.6$  mm/s for the test with  $\gamma=1$ , and  $98.7 \pm 2.8$  mm/s for  $\gamma=5$ . The position error is showed in Fig. 5-B. Subplot C of Fig. 5 presents the position error as a function of  $\beta$  with  $\gamma=1$ . Decreasing  $\beta$  reduces the position error; however, the swimmer velocity along the path also decreases. Subplot D is a plot of the position error as a function of  $\gamma$  with  $\beta=3.5$ . This curve presents a minimum at  $\gamma=5$ .

#### B. Blood clot removal experiments

Blood clot removal tests were performed at 45 Hz for four different swimmer designs in accordance with the experimental protocol described in Section II. Table I summarizes the results. Designs A and C produced relatively low removal rates ( $0.3 \text{ mm}^3/\text{min}$  and  $1.76 \text{ mm}^3/\text{min}$ , respectively). The drill bit tip of swimmer C quickly penetrated the clot, but clot removal progress slowed significantly once the diamond-coated surface touched the clot. Design B and D demonstrated higher removal rates. The low removal rate of designs A and C could be explained by the fact that their tips have a large surface area, which reduces the pressure applied to the clot. Blood clots are made of a fibrin fiber network. These agents compress a large section of the blood clot but exert insufficient pressure to make the diamond grains penetrate between the fibers of the clot, resulting in poor abrading performance. Designs B and D have a smaller surface that applies a larger and non-uniform pressure on the clot. This applies greater mechanical stress on the blood clot and makes the diamond grains penetrate deeper within the fibers, which results in higher removal rates. Swimmers with sharp edges can stick in the clot if the edges penetrate too deep. However, if a tip is too smooth, the removal rate is low. The removal rate of Design B at 45 Hz was measured at  $12.3 \text{ mm}^3/\text{s}$ . For comparison, streptokinase (thrombolytic medication) was found to remove blood clots at a rate of  $0.17 \text{ mm}^3/\text{s}$  in channels of similar size [32]. Design D became stuck in the blood clot and stopped rotating when approximately 20% of the clot was left. It did not successfully remove the blood clot despite a fast initial removal rate.

The removal rate of design B was further characterized by performing clot removal at different rotational speeds  $R_s$  between 35 and 50 Hz. A plot of the obtained removal rates ( $R_r$ ) is presented in Fig. 1 and pictures of a representative removal experiment are shown in Fig. 6. Three measurements were made for each rotational speed.

The blood clot removal rate increases when the rotational speed is increased. The relationship between  $R_r$  and  $R_s$  is approximately linear and can be approximated by  $R_r = 0.904 \cdot R_s - 30.1$  with a coefficient of determination  $R^2=0.76$ . The maximum removal rate ( $20.13 \text{ mm}^3/\text{min}$ ) was observed at the largest tested rotational speed (50 Hz). Swimmer B was able to completely remove all the clots made to construct this plot. The measured values of removal rate present some discrepancy, which is reflected in the relatively low  $R^2$  value. Experiments were performed over a time span of three weeks. The blood was taken from a single volunteer, but this was not sufficient to ensure that all blood clots have the same properties. During the manipulation of the blood samples, it was observed that some days the blood coagulated faster than others. On the plot of Fig. 1, it can be seen that measurements made at 37.5, 42.5, and 47.5 Hz seem to be aligned on a linear curve that has a lower slope than for the other points. Data at 35, 40, 45, and 50 Hz were measured first, and the other points were added later to increase the resolution of the plot. The lower removal rate observed for these points might be due to the variations of the blood clot properties or to the wear of the device. The step-out frequency was approximately equal to 55 Hz during the experiments made to construct the plot of Fig. 1. The measurements were performed at rotational speeds lower than this value and, therefore, the swimmer did not step out of magnetic field synchronization during the experiments.

### IV. COMBINED 3D NAVIGATION AND BLOOD CLOT REMOVAL

Separate experiments showed that swimmer B is able to perform 3D navigation (see Section III-A) and abrade blood clots efficiently (see Section III-B). This last section combines both capabilities in a single experiment. For this test, a 3 mm tube was attached perpendicular to a 15 mm tube using epoxy resin. Both tubes are transparent to allow visual feedback of the swimmer's position. The assembly was held inside the workspace by two plastic supports. The 15 mm tube is oriented vertically at the center of the workspace (see Fig. 7). A blood clot was made inside the 3 mm tube by following the protocol described in Section II-E. The workspace was filled with PBS solution, which had been heated to  $37^\circ\text{C}$  using an induction stove. A cylindrical box having a diameter and height both equal to 15 mm was present at the bottom of the workspace and was used to prevent the swimmer from moving in the workspace between each test. It ensured that the swimmer always started the navigation at the same location. The swimmer was programmed to exit the box, enter the 15 mm tube from the bottom, and progress upward. It then made a sharp turn to enter the 3 mm tube. The controller described in Section II-D



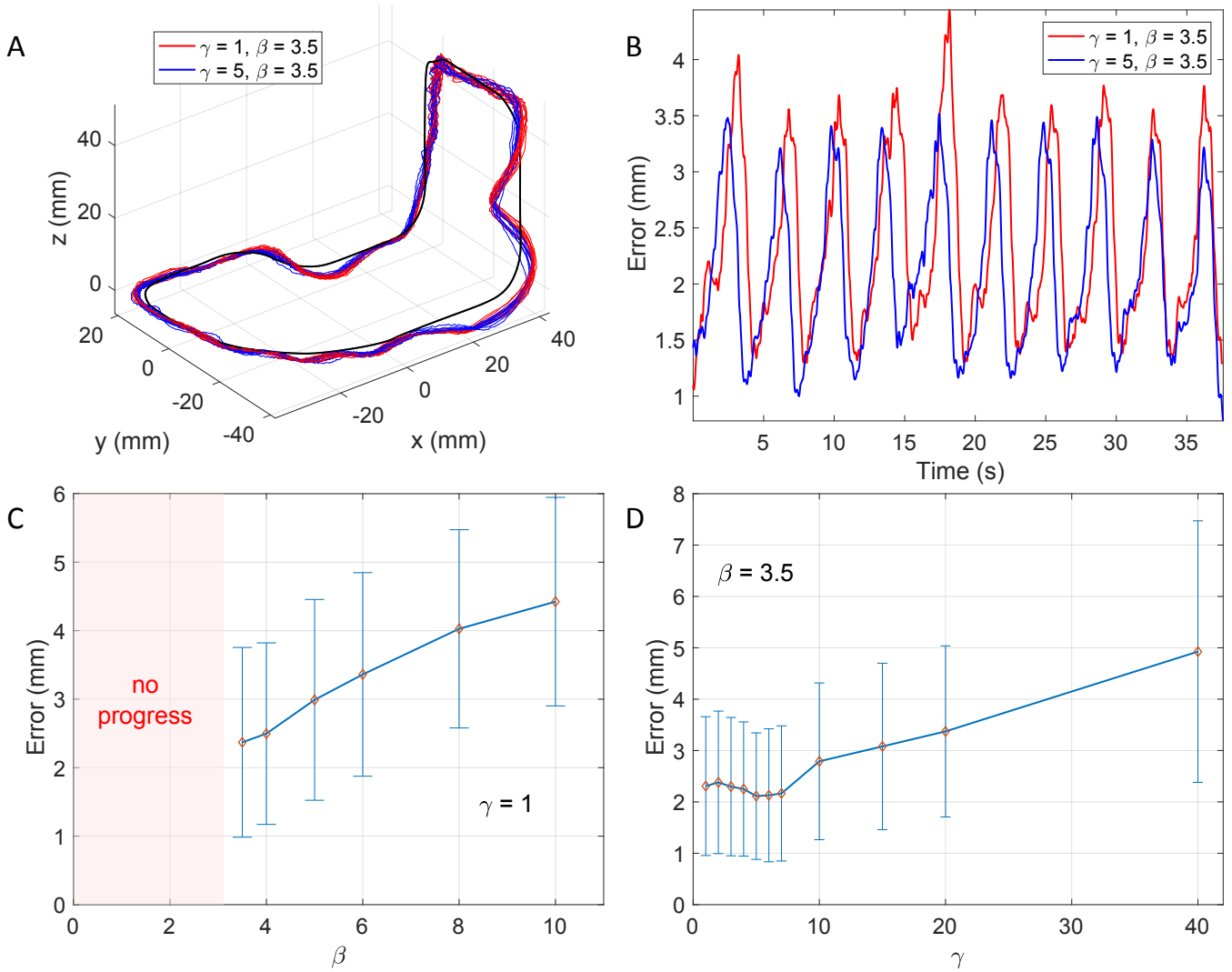


Fig. 5. Path-following results. (A) 3D path-following trajectories with two sets of parameter values. The corresponding path-following errors are shown in (B). (C) and (D) show parameter sweeps for  $\gamma$  and  $\beta$ . Each data point represents 10 laps around the path. The best result is achieved when  $\gamma = 5$  and  $\beta = 3.5$ .

was used with  $\gamma = 1$  and  $\beta = 4$ . These values were chosen after several experimental tests, and enable a smooth entry inside the 3 mm tube. The system was switched to open-loop control when the swimmer contacted the blood clot. The magnetic field was set to rotate at a constant frequency of 45 Hz. The blood clot was removed after 161 s of rubbing. Pictures from a video of the experiment are presented in Fig. 7. A video of the experiment is attached to this paper. This test experimentally demonstrates for the first time that a magnetic swimmer can perform both 3D navigation and blood clot removal during the same experiment.

## V. DISCUSSION

The experiments showed that millimeter-scale robots can navigate 3D paths with an average error of 2.3 mm. Similar prototypes were described in [39] and can reach velocities of up to 100 mm/s, enabling counter-flow navigation in arteries outside the heart and aorta. Experiments showed that these magnetic robots can remove blood clots at rates of up to

20.13 mm<sup>3</sup>/min. This is the first successful complete removal of clots in vitro by a magnetically-propelled tetherless robot. The removal rate is significantly higher than the values currently reported in the literature. High removal rates are needed because ischemia causes tissue to lack oxygen, and irreversible damages can occur quickly. The probability of good clinical outcome decreases as the time taken for vessel reperfusion increases. Recanalization does not improve the patient's outcome if performed after 7 hours [41].

As shown in Section IV, our miniature swimmer can navigate inside a tube, having a diameter of 15 mm without touching the walls. This is less than the diameter of the ascending aorta. Not touching the walls of the aorta would prevent plaque detachment or disturbances of the endothelium. Miniature swimmers could reduce infection risk and recovery time, improve patient outcomes and comfort, and provide treatment options for inoperable clots. Blood clot removal could be performed inside large vessels like the

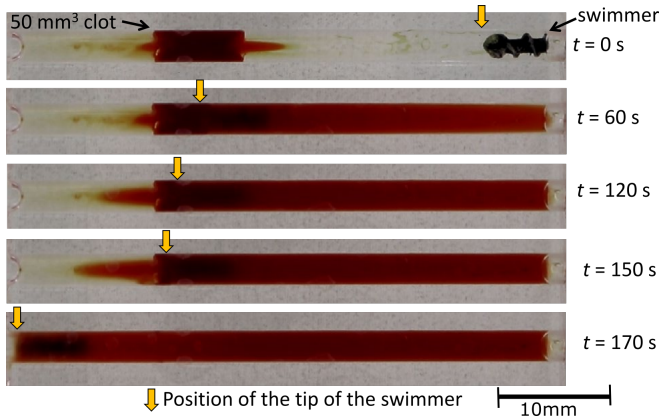


Fig. 6. Pictures of a rotating swimmer removing a human blood clot inside a PDMS channel. The trial corresponds to swimmer B (see Table I), but tested at 50 Hz.

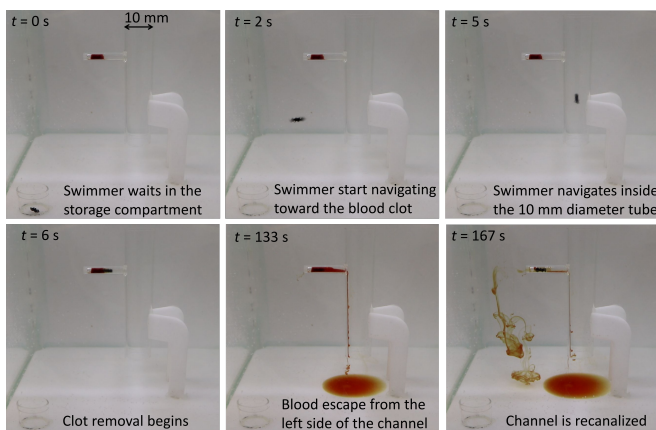


Fig. 7. Images from a video showing the miniature swimmer performing the combined 3D closed-loop path following and blood clot removal experiment. The video is available as multimedia material attached to this paper.

pulmonary arteries. Clots could also be removed in smaller vessels. Preventing the swimmer from touching the walls of small vessels is challenging. The swimmers presented in this paper have a diameter of 2.5 mm and a length of 6 mm. This size could allow the insertion of the swimmer within the bloodstream of a patient using conventional catheter insertion methods [42]. In our study, blood clots are removed from channels that are only slightly larger than the swimmer (3 mm diameter). Our experimental setup does not regulate the radial position of the swimmer inside the channel during the clot removal and, therefore, the swimmer's sides do rub against the walls of the channel. The effect of this rubbing action on the endothelium is not investigated in the present paper. It should be noted that the damage to the vessels might be minimal because no significant force is applied by the swimmer in the radial direction (direction perpendicular to the vessel wall). Additionally, the abrasive coating is only present at the tip of the swimmer and would, therefore, not be in contact with the artery walls during clot removal.

**Future Work:** These results are promising but preliminary. Additional work addressing imaging modalities, system latency, blood flow, and properties of tissue and blood clots

are required to achieve successful in vivo navigation. **Sensing:** This work used cameras for localization, but because the human body is mostly opaque, applications must use a different imaging modality such as MRI, X-ray, CT, or ultrasound imaging. **Modify workspace:** This study used no flow, but treatment plans and controllers are needed for pulsatile flow. More complicated 3D curved vascular channels can better test the controller system, and allow for effective simulation of real clots. Simple enhancements can include vertical channels for clot removal, and branched channels for navigation. Forming clots in complex channels will require new techniques. Future work must investigate swimmer insertion and retrieval. **Modify swimmer:** The current size of the swimmers precludes navigation through the entire vascular system, as capillary beds, and their accompanying arterio-venous anastomoses are not big enough for the swimmers. Future work could focus on downscaling the swimmer and optimizing the design. **Modify clot:** Additional experiments could vary the composition of the thrombi created to emulate more real-life conditions. The clots used were composed entirely of normal human blood, and contain little to no fat that would be found in patients with different diets and atherosclerosis. Blood samples from patients predisposed to certain vascular diseases, as well as those who have certain conditions, could better predict the real-world effectiveness of such a swimmer.

#### ACKNOWLEDGMENT

This work was supported by the National Science Foundation under Grants No. [IIS-1553063], [IIS-1619278], [CNS-1932572] and [CNS-1646566]. A provisional patent application was filed as U.S. App. No. 62/778,671.

#### REFERENCES

- [1] L. J. J. Scheres, W. M. Lijfering, and S. C. Cannegieter, "Current and future burden of venous thrombosis: Not simply predictable," *Research and Practice in Thrombosis and Haemostasis*, vol. 2, no. 2, pp. 199–208, 2018. [Online]. Available: <https://onlinelibrary.wiley.com/doi/abs/10.1002/rth2.12101>
- [2] D. D. Ribeiro, W. M. Lijfering, S. M. Barreto, F. R. Rosendaal, and S. M. Rezende, "Epidemiology of recurrent venous thrombosis," *Brazilian journal of medical and biological research*, vol. 45, no. 1, pp. 1–7, 2012.
- [3] I. A. Næss, S. Christiansen, P. Romundstad, S. Cannegieter, F. R. Rosendaal, and J. Hammerstrøm, "Incidence and mortality of venous thrombosis: a population-based study," *Journal of thrombosis and haemostasis*, vol. 5, no. 4, pp. 692–699, 2007.
- [4] M. Cushman, "Epidemiology and risk factors for venous thrombosis," *Seminars in hematology*, vol. 44, no. 2, pp. 62–69, 2007.
- [5] V. Tagalakis, V. Patenaude, S. R. Kahn, and S. Suissa, "Incidence of and mortality from venous thromboembolism in a real-world population: the q-vte study cohort," *The American journal of medicine*, vol. 126, no. 9, pp. 832–e13, 2013.
- [6] J. A. Heit, "The epidemiology of venous thromboembolism in the community," *Arteriosclerosis, thrombosis, and vascular biology*, vol. 28, no. 3, pp. 370–372, 2008.
- [7] A. M. Wendelboe and G. E. Raskob, "Global burden of thrombosis," *Circulation Research*, vol. 118, no. 9, pp. 1340–1347, 2016. [Online]. Available: <https://www.ahajournals.org/doi/abs/10.1161/CIRCRESAHA.115.306841>
- [8] C. Castaño, L. Dorado, C. Guerrero, M. Millán, M. Gomis, N. Perez de la Ossa, M. Castellanos, M. R. García, S. Domenech, and A. Dávalos, "Mechanical thrombectomy with the solitaire ab device in large artery occlusions of the anterior circulation: a pilot study," *Stroke*, vol. 41, no. 8, pp. 1836–1840, 2010.

- [9] W. S. Smith, G. Sung, J. Saver, R. Budzik, G. Duckwiler, D. S. Liebeskind, H. L. Lutsep, M. M. Rymer, R. T. Higashida, S. Starkman *et al.*, "Mechanical thrombectomy for acute ischemic stroke: final results of the multi merci trial," *Stroke*, vol. 39, no. 4, pp. 1205–1212, 2008.
- [10] J. E. Delgado Almandoz, Y. Kayan, M. L. Young, J. L. Fease, J. M. Scholz, A. M. Milner, T. H. Hehr, P. Roohani, M. Mulder, and R. M. Tarrel, "Comparison of clinical outcomes in patients with acute ischemic strokes treated with mechanical thrombectomy using either solumbra or adapt techniques," *Journal of NeuroInterventional Surgery*, vol. 8, no. 11, pp. 1123–1128, 2016. [Online]. Available: <https://jn.is.bmj.com/content/8/11/1123>
- [11] E. Zeitler, W. Schoop, and W. Zahnow, "The Treatment of Occlusive Arterial Disease by Transluminal Catheter Angioplasty," *Radiology*, vol. 99, no. 1, pp. 19–26, apr 1971. [Online]. Available: <http://pubs.rsna.org/doi/10.1148/99.1.19>
- [12] G. Thomalla, C. Schwark, J. Sobesky, E. Bluhmki, J. B. Fiebach, J. Fiehler, O. Zaro Weber, T. Kucinski, E. Juettler, P. A. Ringleb *et al.*, "Outcome and symptomatic bleeding complications of intravenous thrombolysis within 6 hours in MRI-selected stroke patients: comparison of a german multicenter study with the pooled data of atlantis, ecass, and ninds tpa trials," *Stroke*, vol. 37, no. 3, pp. 852–858, 2006.
- [13] S. Schulman, R. J. Beyth, C. Kearon, and M. N. Levine, "Hemorrhagic complications of anticoagulant and thrombolytic treatment: American college of chest physicians evidence-based clinical practice guidelines," *Chest*, vol. 133, no. 6, pp. 257S–298S, 2008.
- [14] M. Hamon, J.-C. Baron, F. Viader, and M. Hamon, "Periprocedural Stroke and Cardiac Catheterization," *Circulation*, vol. 118, no. 6, pp. 678–683, aug 2008. [Online]. Available: <https://www.ahajournals.org/doi/10.1161/CIRCULATIONAHA.108.784504>
- [15] P. Khatri and S. E. Kasner, "Ischemic Strokes After Cardiac Catheterization," *Archives of Neurology*, vol. 63, no. 6, p. 817, jun 2006.
- [16] W. Hu, G. Z. Lum, M. Mastrangeli, and M. Sitti, "Small-scale soft-bodied robot with multimodal locomotion," *Nature*, vol. 554, no. 7690, p. 81, 2018.
- [17] K. Vollmers, D. R. Frutiger, B. E. Kratochvil, and B. J. Nelson, "Wireless resonant magnetic microactuator for untethered mobile microrobots," *Applied Physics Letters*, vol. 92, no. 14, p. 144103, apr 2008. [Online]. Available: <http://aip.scitation.org/doi/10.1063/1.2907697>
- [18] O. Onaizah and E. Diller, "Tetherless mobile micro-surgical scissors using magnetic actuation," in *2019 International Conference on Robotics and Automation (ICRA)*. IEEE, 2019, pp. 894–899.
- [19] I. S. M. Khalil, D. Mahdy, A. E. Sharkawy, R. R. Moustafa, A. F. Tabak, M. E. Mitwally, S. Hesham, N. Hamdi, A. Klingner, A. Mohamed, and M. Sitti, "Mechanical Rubbing of Blood Clots Using Helical Robots Under Ultrasound Guidance," *IEEE Robotics and Automation Letters*, vol. 3, no. 2, pp. 1112–1119, apr 2018. [Online]. Available: <http://ieeexplore.ieee.org/document/8253812/>
- [20] I. S. M. Khalil, A. F. Tabak, K. Sadek, D. Mahdy, N. Hamdi, and M. Sitti, "Rubbing Against Blood Clots Using Helical Robots: Modeling and In Vitro Experimental Validation," *IEEE Robotics and Automation Letters*, vol. 2, no. 2, pp. 927–934, apr 2017. [Online]. Available: <http://ieeexplore.ieee.org/document/7820160/>
- [21] I. S. Khalil, D. Mahdy, A. El Sharkawy, R. R. Moustafa, A. F. Tabak, M. E. Mitwally, S. Hesham, N. Hamdi, A. Klingner, A. Mohamed *et al.*, "Mechanical rubbing of blood clots using helical robots under ultrasound guidance," *IEEE Robotics and Automation Letters*, vol. 3, no. 2, pp. 1112–1119, 2018.
- [22] D. Mahdy, R. Reda, N. Hamdi, and I. S. Khalil, "Ultrasound-guided minimally invasive grinding for clearing blood clots: promises and challenges," *IEEE Instrumentation & Measurement Magazine*, vol. 21, no. 2, pp. 10–14, 2018.
- [23] F. Ullrich, F. Qiu, J. Pokki, T. Huang, S. Pane, and B. J. Nelson, "Swimming characteristics of helical microrobots in fibrous environments," in *2016 6th IEEE International Conference on Biomedical Robotics and Biomechanics (BioRob)*. IEEE, jun 2016, pp. 470–475. [Online]. Available: <http://ieeexplore.ieee.org/document/7523671/>
- [24] A. Hosney, A. Klingner, S. Misra, and I. S. M. Khalil, "Propulsion and steering of helical magnetic microrobots using two synchronized rotating dipole fields in three-dimensional space," in *2015 IEEE/RSJ International Conference on Intelligent Robots and Systems (IROS)*. IEEE, sep 2015, pp. 1988–1993. [Online]. Available: <http://ieeexplore.ieee.org/document/7353639/>
- [25] T. Xu, G. Hwang, N. Andreff, and S. Regnier, "Planar Path Following of 3-D Steering Scaled-Up Helical Microswimmers," *IEEE Transactions on Robotics*, vol. 31, no. 1, pp. 117–127, feb 2015. [Online]. Available: <http://ieeexplore.ieee.org/document/7015549/>
- [26] A. W. Mahoney, J. C. Sarrazin, E. Bamberg, and J. J. Abbott, "Velocity control with gravity compensation for magnetic helical microswimmers," *Advanced Robotics*, vol. 25, no. 8, pp. 1007–1028, 2011.
- [27] W. Lee, S. Jeon, J. Nam, and G. Jang, "Dual-body magnetic helical robot for drilling and cargo delivery in human blood vessels," *Journal of Applied Physics*, vol. 117, no. 17, p. 17B314, may 2015. [Online]. Available: <http://aip.scitation.org/doi/10.1063/1.4917067>
- [28] T. Xu, G. Hwang, N. Andreff, and S. Regnier, "Characterization of three-dimensional steering for helical swimmers," in *2014 IEEE International Conference on Robotics and Automation (ICRA)*. IEEE, may 2014, pp. 4686–4691. [Online]. Available: <http://ieeexplore.ieee.org/document/6907544/>
- [29] A. W. Mahoney, N. D. Nelson, K. E. Peyer, B. J. Nelson, and J. J. Abbott, "Behavior of rotating magnetic microrobots above the step-out frequency with application to control of multi-microrobot systems," *Applied Physics Letters*, vol. 104, no. 14, p. 144101, apr 2014. [Online]. Available: <http://aip.scitation.org/doi/10.1063/1.4870768>
- [30] K. Ishiyama, K. Arai, M. Sendoh, and A. Yamazaki, "Spiral-type micro-machine for medical applications," in *MHS2000. Proceedings of 2000 International Symposium on Micromechatronics and Human Science (Cat. No.00TH8530)*. IEEE, 2000, pp. 65–69. [Online]. Available: <http://ieeexplore.ieee.org/document/903292/>
- [31] W. Gao, X. Feng, A. Pei, C. R. Kane, R. Tam, C. Hennessy, and J. Wang, "Bioinspired Helical Microswimmers Based on Vascular Plants," *Nano Letters*, vol. 14, no. 1, pp. 305–310, jan 2014. [Online]. Available: <http://pubs.acs.org/doi/10.1021/nl404044d>
- [32] I. S. Khalil, A. F. Tabak, K. Sadek, D. Mahdy, N. Hamdi, and M. Sitti, "Rubbing against blood clots using helical robots: modeling and in vitro experimental validation," *IEEE Robotics and Automation Letters*, vol. 2, no. 2, pp. 927–934, 2017.
- [33] S. Lee, S. Lee, S. Kim, C.-H. Yoon, H.-J. Park, J.-y. Kim, and H. Choi, "Fabrication and characterization of a magnetic drilling actuator for navigation in a three-dimensional phantom vascular network," *Scientific reports*, vol. 8, no. 1, p. 3691, 2018.
- [34] X. Wu, J. Liu, C. Huang, M. Su, and T. Xu, "3-d path following of helical microswimmers with an adaptive orientation compensation model," *IEEE Transactions on Automation Science and Engineering*, 2019.
- [35] A. Oulmas, N. Andreff, and S. Régnier, "3d closed-loop swimming at low reynolds numbers," *The International Journal of Robotics Research*, vol. 37, no. 11, pp. 1359–1375, 2018.
- [36] H. Zhao, L. Julien, M. Feucht, O. Bailey, and A. Becker, "3d path-following using mrac on a millimeter-scale spiral-type magnetic robot," *IEEE Robotics and Automation Letters*, pp. 1–1, 2020.
- [37] J. Leclerc, B. Isichei, and A. T. Becker, "A magnetic manipulator cooled with liquid nitrogen," *IEEE Robotics and Automation Letters*, vol. 3, no. 4, pp. 4367–4374, 2018.
- [38] J. C. Simpson, J. E. Lane, C. D. Immer, R. C. Youngquist, and T. Steinrock, "Simple Analytic Expressions for the Magnetic Field of a Circular Current Loop," *NASA/TM-2013-217919*, jan 2001. [Online]. Available: <https://ntrs.nasa.gov/search.jsp?R=20010038494>
- [39] J. Leclerc, H. Zhao, and A. T. Becker, "3d control of rotating millimeter-scale swimmers through obstacles," in *2019 International Conference on Robotics and Automation (ICRA)*, 2019, pp. 8890–8896.
- [40] N. Korin, M. Kanapathipillai, B. D. Matthews, M. Crescente, A. Brill, T. Mammoto, K. Ghosh, S. Jurek, S. A. Bencherif, D. Bhatta *et al.*, "Shear-activated nanotherapeutics for drug targeting to obstructed blood vessels," *Science*, p. 1217815, 2012.
- [41] P. Khatri, T. Abruzzo, S. Yeatts, C. Nichols, J. Broderick, T. Tomsick *et al.*, "Good clinical outcome after ischemic stroke with successful revascularization is time-dependent," *Neurology*, vol. 73, no. 13, pp. 1066–1072, 2009.
- [42] E. Hulse and G. Thomas, "Vascular access on the 21st century military battlefield," *Journal of the Royal Army Medical Corps*, vol. 156, pp. 385–90, 12 2010.